Large Eddy Simulation of a High Subsonic Jet and Noise Generation

Yuya FUKUDA, Susumu TERAMOTO and Toshio NAGASHIMA
Department of Aeronautics and Astronautics, School of Engineering, University of Tokyo
Engineering Bld. #7, Hongo 7-3-1, Bunkyo, Tokyo 113-8656, Japan
fukuda@thermo.t.u-tokyo.ac.jp

Keywords: Computational Aeroacoustics, Jet Noise, Large Eddy Simulation

Abstract

For the purpose of improving accuracy in jet noise prediction and investigating its generation mechanism, high subsonic jets were computed by using compressible Large Eddy Simulation (LES), wherein the inflow forcing or disturbance added in the inflow shear layer was incorporated. The far-field Sound Pressure Levels (SPL) as well as the flow field resulted in good agreement with available experimental data by applying only the high azimuthal modes among the inflow forcing parameters. We found that this result was due to an important role of the inflow forcing upon breaking down the axiymmetric vortices that caused high amplitude velocity and pressure fluctuations. In order to examine generation mechanism of the dominant noise component, wavelet transformation was introduced to reveal the presence of a well-organized structure of pressure fluctuations that originated mainly from vortex motions near the end of the jet potential core. This structure took a train of alternately positive and negative wavelet-transformed pressure regions along the jet distance, spreading towards the downstream with advection and propagation. It was concluded that this structure and its dynamic motion are the reason why a high subsonic jet produces the dominant noise with a particular downstream directivity.

Introduction

Since jet noise remains an important source of aircraft noise at take off and the number of commercial aircrafts is continuously increasing, reduction of jet noise continues to be a crucial issue. In order to develop more quiet nozzles, it is important to improve accuracy in jet noise prediction and to understand its generation mechanism.

By many studies[1-5], dominant noise of a high subsonic jet has been indicated to be the noise with angular angle near 30 degrees measured from the jet axis and frequency range corresponding to Strouhal number, St, of 0.2 to 0.5. In addition, the dominant jet noise has been shown to originate from a region near the end of the jet potential core[6-11].

In order to understand the noise generation mechanism, a significant amount of work has been devoted for more than 50 years. Lighthill[12] made the first significant contribution to our understanding of how sound is produced by turbulence. This was achieved by reformation of the governing equations of fluid dynamics into a form analogous to the wave equation. About the turbulence, Powell[13] suggested that unsteady vortices motions were the major sources of sound. Lighthill suggested the eighth power law by thinking that a jet was filled with small vortices with small wavelength compared to that of sound and they generated sounds independently. Though far-field Sound Pressure Levels (SPL) obtained by this model agreed well with experimental data for low Mach number jets, this model could not explain the reason why the jet has the downstream directivity and the frequency characteristics. Meanwhile, Mollo-Christensen[14] suggested that the jet itself had large-scale structures, because its pressure fluctuation had had high coherency. The presence of this large-scale coherent structures was confirmed also by Crow et al.[15-16] As a model to explain a relation between this large-scale coherent structures and the noise generation, Crow[17] suggested that waves on the jet generated sounds as a whole. This model, however, could not explain streamwise distribution of noise sources obtained by experiments. To resolve this contradiction, Laufer et al.[18-19] suggested that interactions of large-scale vortex rings generated sound. In addition, Morrison et al.[7] suggested that the noise generation was ascribed to a rapid decay of the dominant instability waves involving a relatively “violent fluid dynamic action” that could be attributed to a vortex interaction.

Recently, in order to understand the relation between large-scale structures and the noise generation, Hileman et al.[20-22] developed experimental techniques that can measure simultaneously the flow field and far-field sound. In this technique, origins of high amplitude sound waves were located using a beamforming algorithm with a three dimensional microphone array. Besides, the flow field was captured by a sheet of light created by a high-power pulsed laser. A proper orthogonal decomposition (POD) was then used to reconstruct dominant flow features during the noise generation. As a result, rapid breakdown of the large-scale structures was observed during noise generation. Kastner et al. [23] included this technique in the direct numerical simulation (DNS) for low Reynolds number jet. They showed that two characteristic phenomena dominated the instantaneous jet pressure and vorticity field during noise generation. The first was an interaction between the two sides of the shear layers, and the second was the breakdown of prominent large-scale structures. By these results, the strong relation between the large-scale structure and the noise generation was confirmed to exist independent of Reynolds number. However, the reason has not been

well cleared why the large-scale structures generate the major noise that has the downstream directivity and the characteristic frequency range.

In addition to experiments, a lot of numerical simulations have been performed because of the complexity of the noise-generation phenomena. As a method of numerical simulation, Large Eddy Simulation (LES) has been applied because it can be used at higher Reynolds number than DNS on a same computational grid. However, in LES, real nozzle exit conditions can not be reproduced unless the Reynolds numbers are kept very low because the discretization of the shear layer leads to a prohibitive number of grid points. Inflow conditions must therefore be modeled. As a model of the inflow turbulence, some forcing of the jet has been used to promote natural transition from an initially quasi-laminar annular shear layer[24]. Bogey et al. applied randomized perturbations in the form of induced velocities from a vortex ring[25] and investigated the effects of its inflow conditions[26]. The results showed that the parameter that had the greatest impact was the number of the azimuthal forcing modes. By removing low modes out of several forcing modes, they found that the simulation resulted in a quieter jet compared to a baseline case with all modes turned on. Lew et al.[27] also investigated the effects of the inflow forcing. Nevertheless, the reason why inflow forcing changes the far-field SPL has not been well clarified. Thus, in most of today's LES, initial parameters defining inflow forcing have been determined so as the simulation results to become close to experimental data. For improving noise estimation accuracy and understanding the noise generation mechanism, which also requires high estimation accuracy, it is desirable to understand how the inflow forcing changed the flow field and the far-field SPL.

The present paper is organized as follows. First, the influence of inflow forcing conditions on the jet development and the far-field SPL are investigated. Second, the reason why they can make the difference on the flow and sound field are investigated by analyzing each vortex structure. Finally, the noise generation mechanism is discussed by showing the dominant structure of the dominant pressure fluctuations using wavelet transformation.

Numerical Methods

Flow Condition

The simulated jets are unheated subsonic circular ones. The Mach number is 0.9. The Reynolds number based on the nozzle exit diameter and the jet velocity at the nozzle exit plane, Re_D, is 2×10^4.

Numerical Schemes

Compressible Large Eddy Simulations are performed by solving the Favre filtered Navier-Stokes equations. As a subgrid scale model, the dynamic Smagorinsky model[28-30] is used. The convective fluxes are evaluated by using a sixth-order compact scheme proposed by Lele[31]. In order to avoid numerical instability, physical properties are filtered using tenth-order implicit spatial filter proposed by Gaitonde and Visbal[32]. The viscous fluxes are evaluated by using the fourth-order central difference scheme. The fourth-order Runge-Kutta scheme is used for time advancement.

Computational Grid

The computational grid is shown in Fig. 1. An O-type grid is used to obtain high grid density around the shear layer. The computational domain is defined by $0 \le x/r_0 \le 60$ and $0 \le r/r_0 \le 15$ where r_0 is the nozzle exit radius. The number of the grid points is equal to $331\times117\times96$ in the axial, radial, and circumferential direction respectively. The radial grid spacing Δ_r at the shear layer is chosen to be $0.01r_0$.

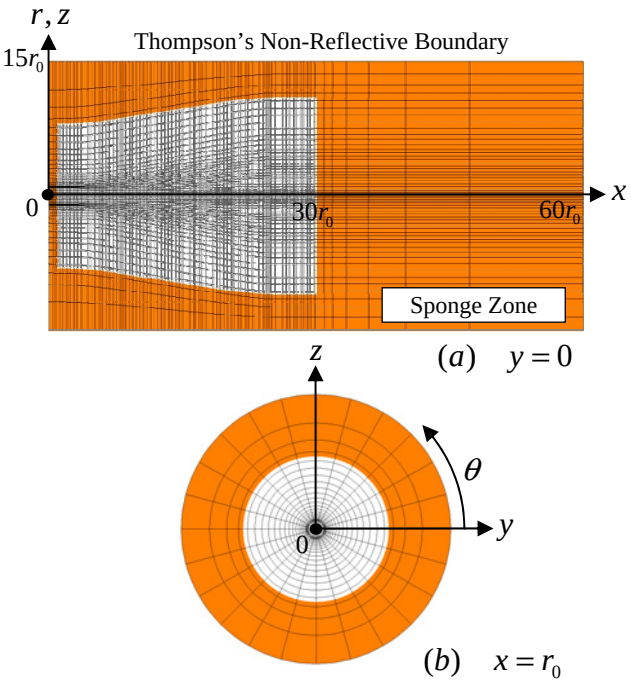

Fig. 1 Cross sections of the computational grid (Every four grid point is shown.)

Boundary Condition

A boundary layer near the jet exit is very thin and the number of points necessary for its discretization would be exorbitant. Therefore, in the present simulation, inflow conditions are modeled by imposing mean flow profiles and ring vortex excitation[25] to seed turbulence. The inflow mean longitudinal velocity $u(r)$ is given by the following profile

$$u(r) = \frac{u_j}{2} + \frac{u_j}{2}\tanh\left(\frac{r_0 - r}{2\delta_\theta}\right) \tag{1}$$

where u_j is the inflow centerline velocity and δ_θ is the initial momentum thickness of the annular shear layer, given here by $\delta_\theta = 0.03r_0$. Static pressure at the nozzle exit is taken as the ambient pressure. The inflow mean density profile is determined by the Crocco-Busemann relation.

Thompson's non-reflective boundary condition[33-34] is used to minimize the amplitude of the acoustic waves reflected at the limits of the computational domain. In addition, sponge zone is added around the jet flow region to attenuate outgoing waves. In this sponge zone shown as the orange area in Fig. 1, grid spacing is extended gradually and an artificial dumping term proposed by Freund[35] is added. The singularity at the centerline is treated by a method proposed by Mohseni and Colonius[36].

Inflow Forcing Parameters

Randomized perturbations in the form of induced velocities from a vortex ring[25] are added to the velocity profile in the shear zone at $x = r_0$. They are divergence-free and low amplitude in order to minimize spurious acoustic waves. This inflow forcing is based on a combination of jet azimuthal modes, and it modifies the flow velocities every time step as follows

$$\begin{pmatrix} u_x' \\ u_r' \end{pmatrix} = \alpha u_j \sum_{i=n}^{m} \varepsilon_i \cos(i\theta + \phi_i) \times \frac{2r_0}{r\Delta} \exp\left(-\ln 2 \frac{(x-x_0)^2 + (r-r_0)^2}{\Delta^2} \right) \begin{pmatrix} r - r_0 \\ x_0 - x \end{pmatrix} \quad (2)$$

where the amplitudes $-1 \le \varepsilon_i \le 1$ and the phases $0 \le \phi_i < 2\pi$ of each mode are randomly updated every iteration. The index i denotes the azimuthal mode number with $i = 0$ being the axisymmetric mode. The parameter α determines the amplitude of the forcing. Though Δ was originally defined as a minimum grid spacing in the shear layer, for our case it is set equal to $0.0313 r_0$ so as to be the same value used by Bogey et al.[25] Hence, the same α represents the same forcing amplitude used by them. x_0 is the axial location of the center of the vortex ring. r_0 is the radius of the vortex ring and here set equal to the initial jet radius.

Since there is no apparent consensus regarding the appropriate parameters of the inflow forcing[24], the choice of these parameter sets is somewhat arbitrary. For instance, Bogey et al.[25] used $\alpha = 0.01$ and $i = 0, \cdots, 9$, whereas Pan et al.[37] used $\alpha = 0.007$ and $i = 4, \cdots, 15$. In the present study, five simulations are carried out with the inflow conditions summarized in Table 1. Three parameters are varied, which are the mode i, the amplitude α, and the application range. The magnitudes of the velocity fluctuations, u'_{rms} / u_j, generated by this forcing are between 3×10^{-4} and 5×10^{-4} at $x = r_0$ and $r = r_0$.

Table 1 Inflow conditions

Test Case	Mode	α	Application Range
LES base	i=4,…,9	0.01	$0.8 \le r/r_0 \le 1.2$
LES m09	i=0,…,9	0.01	$0.8 \le r/r_0 \le 1.2$
LES weak	i=4,…,9	0.007	$0.8 \le r/r_0 \le 1.2$
LES narrow	i=4,…,9	0.01	$0.9 \le r/r_0 \le 1.1$
LES none	Without inflow forcing		

Kirchhoff Method

SPL at the far-field observer locations are evaluated from Kirchhoff surface integration[38-40]. The integral relation is given by

$$p'(\mathbf{y},t) = \frac{1}{4\pi} \iint \left[\frac{p'}{r^2} \frac{\partial r}{\partial n} - \frac{1}{r} \frac{\partial p'}{\partial n} + \frac{1}{c_\infty r} \frac{\partial r}{\partial n} \frac{\partial p'}{\partial t} \right]_{\tau_r} dS(\mathbf{x}) \quad (3)$$

where $\mathbf{y}$ is a observer location in the far-field and $\mathbf{x}$ is a location on the Kirchhoff surface, S, which is shown in Fig. 2. $r = |\mathbf{y} - \mathbf{x}|$ is the distance from the surface to the observer. τ_r denotes that the expression within brackets is to be evaluated at retarted time, i.e. emission time. τ_r is related to the observer evaluation time t as $\tau_r = t - r/c_\infty$ where c_∞ is the speed of sound in far-field region.

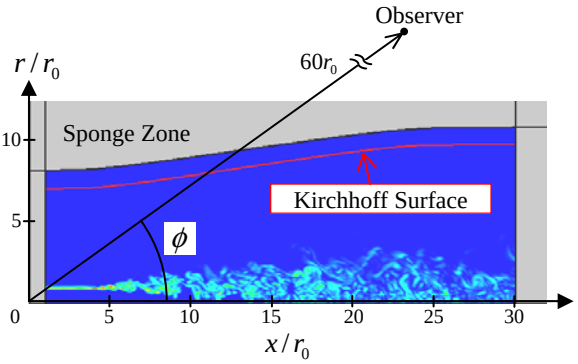

Fig. 2 Kirchhoff surface and observer location

Wavelet Transformation

Wavelet transformation[41-43] allows for the analysis of a signal with varying resolution in time and frequency domains. Therefore, it is a valuable tool for analysing jet noise whose frequency varies with time. The general equation for the wavelet transformation, $X_{wav}(a,b)$, is given as

$$X_{wav}(a,b) = \frac{1}{\sqrt{a}} \int_{-\infty}^{\infty} x(t) \psi^* \left(\frac{t-b}{a} \right) dt \quad (4)$$

where $x(t)$ is the signal to be transformed, ψ is a mother wavelet used to analyze the signal, and * denotes the complex conjugate. After the transformation, the signal is in a domain of translation b and scale a.

The Mexican hat wavelet is a commonly used wavelet that is especially well suited to analyze peak locations within a signal. This is because it has a central peak and two small side lobes. The normalized Mexican hat wavelet is given by

$$\psi_{\text{mexh}}(\tau) = \frac{2(1-\tau^2)}{\sqrt{3}\pi^{1/4}} \exp\left(-\frac{\tau^2}{2} \right) \quad (5)$$

where τ is the modified time given by $(t-b)/a$. The time scale a is converted to frequency f by the following relation:

$$f = \frac{\sqrt{5/2}}{2\pi a} \quad (6)$$

which is only valid for the Mexican hat wavelet. This relation can be analytically obtained by matching the

peak of the wavelet mean spectrum with the peak of the Fourier transform of the cosine wave. In the discussion of the results, f is referred to as scale frequency because it is different from the commonly defined frequency from Fourier analysis.

Detailed information on the wavelet transformation can be found in the refrences[41-43].

Noise Source Location Method

Hileman et al.[21-23] used a beamforming algorithm with a three-dimensional microphone array to locate the sources of the intense sound waves. In the present work, a virtual microphone array with large number of microphones and a beamforming algorithm similar to that used by Hileman et al. are used. The virtual microphones are located on the Kirchhoff surface area with $25 \le x/r_0 \le 30$ and $9.68 \le r/r_0 \le 9.72$, which is shown in Fig. 2. This location is for detecting the dominant jet noise, which has a peak at around 30 degrees to the downstream jet axis. The number of the microphones is equal to 51×96 in the axial and circumferential direction respectively.

After a high amplitude noise-generating event in the jet, the sound wave propagates to the far field and eventually reaches the virtual microphone array. Then the sound wave is recorded as a pressure fluctuation. To detect only the dominant jet noise, the wavelet transformation is applied to the pressure fluctuation data with a time scale corresponding to the dominant frequency of the jet noise. Then, the signal is normalized by its standard deviation. The peaks of the acoustic signal with a magnitude above 1.5 are treated as noise generation events.

The time delay is determined by finding the maximum value of the correlation coefficient between two microphone signals. In the present work, refraction effects of the sound waves are neglected and the sound waves are assumed to be spherical waves at the microphone locations. Hence, all 96 microphone pairs with downstream distances of $5r_0$ are used to locate x-components of the noise sources. Microphones within the following range (7) are used to locate y-components and, similarly, microphones within the range (8) are used to locate z-components. Thus, total 51×34 microphone pairs with azimuthal distances of 60 degrees are used to locate the y- and z-components of the noise sources.

$$\frac{1}{6}\pi \le \theta \le \frac{5}{6}\pi,\ \frac{7}{6}\pi \le \theta \le \frac{11}{6}\pi \qquad (7)$$

$$0 \le \theta \le \frac{1}{3}\pi,\ \frac{2}{3}\pi \le \theta \le \frac{4}{3}\pi,\ \frac{5}{3}\pi \le \theta < 2\pi \qquad (8)$$

Further details of the beamforming algorithm can be found in the reference[21].

Influence of inflow conditions

Jet Development

Influence of the inflow forcing on the jet developments is now investigated. Axial profiles of the mean axial velocities along the centerline are plotted in Fig. 3. Besides, root mean square values of the axial fluctuating velocities along the centerline are plotted in Fig. 4. These two figures show that the jet developments for LES base, LES weak, and LES narrow are in a good agreement with experimental data[44-45]. On the contrary, the velocity fluctuation in LES m09 is larger for $x/r_0 < 16$ than that in the above three cases. In addition, the jet develops more rapidly in LES m09 than in the above three case. LES none is the case in which the velocity fluctuation is the largest for $7 < x/r_0 < 22$ and the jet develops the most rapidly. From these results, it is confirmed that without inflow forcing the jet develops more rapidly than in the experiments. This tendency is consistent with the result reported by Bogey et al.[26]

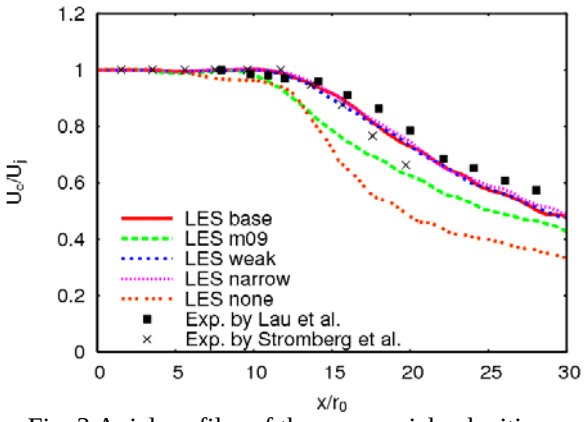

Fig. 3 Axial profiles of the mean axial velocities along the centerline

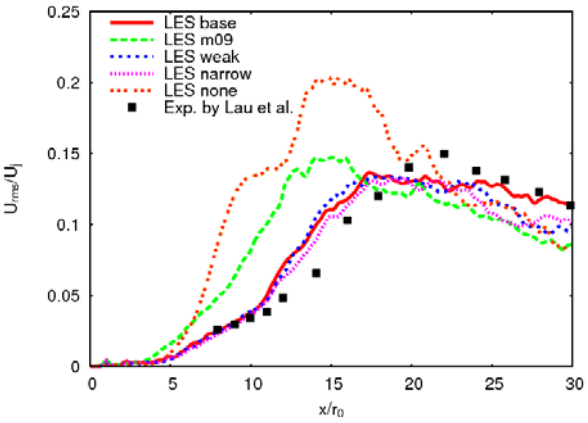

Fig. 4 Axial profiles of the root mean square values of the axial fluctuating velocities along the centerline

Far-Field OASPL

Far-field overall SPL (OASPL) with distances of $60r_0$ from the nozzle exit are compared with experimental data[1,46] in Fig. 5. The angle ϕ is measured relative to the downstream jet axis. This figure show that the OASPL for LES base, LES weak, and LES narrow are in a good agreement with the measurements in terms of, not only the directivity patterns with the peaks at the angle near 30 degrees, but also the levels. On the contrary, OASPL for LES m09 is about 3 dB higher and for LES none about 10 dB higher than that for the measurements.

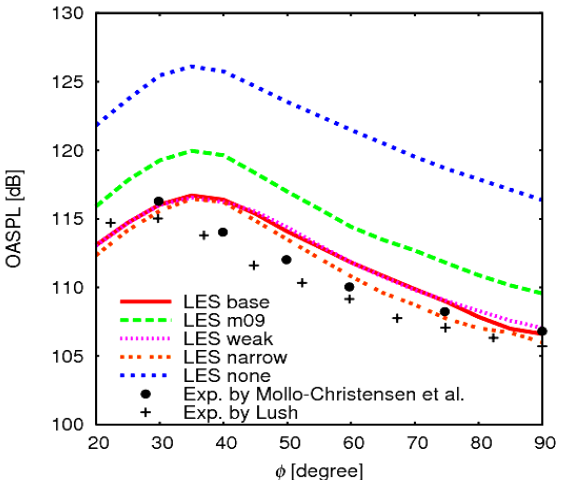

Fig. 5 Overall SPL at $60r_0$ from the nozzle exit

In summary, both the jet development and the far-field OASPL are confirmed to be dependent appreciably on the inflow forcing. The cases with low modes cut, LES base, LES weak, and LES narrow, are shown to be in a good agreement with experimental data in terms of not only the jet development but also the far-field OASPL. The results indicate that inflow forcing reduces the overestimation of the jet development and the far-field OASPL. Furthermore, the effect is dependent significantly on the azimuthal modes of the inflow forcing. On the other hand, the parameters of the forcing amplitude and the application range make no significant difference to the jet development or the far-field OASPL.

In the next section, the mechanisms that the azimuthal modes makes the significant difference on the flow and sound field are investigated for three cases, LES base (Mode 4-9), LES m09 (Mode 0-9), and LES none (None).

Analysis of Inflow Forcing Effect

Vortex Structure

Vortex structures are visualized by iso-surfaces of the second invariant Q of the velocity gradient tensor[47] for None (LES none), Mode 0-9 (LES m09), and Mode 4-9 (LES base). These surfaces are colored according to ω_x. They are shown in Fig. 6. When without inflow forcing, axisymmetric vortex rings are observed. These vortex rings move downstream and disintegrate, accompanying large scale streamwise vortices. On the other hand, when inflow forcing is added, the vortices at the shear layer are distorted. Fig. 6b and Fig. 6c show that for Mode 0-9, distorted vortex rings are formed, while for Mode 4-9, there are only small vortices divided in the circumferential direction.

These results reveal that the inflow forcing has a role to break down the axisymmetric vortices. This phenomenon is attributed to the velocity fluctuation given by the inflow forcing that is very small but differs in the circumferential direction. The difference of vortex structures between Mode 0-9 and Mode 4-9 is seem to be due to the difference of the proportion of high modes to the whole modes.

For the case without inflow forcing, axiymmetric vortices appear to within about $5 < x/r_0 < 8$ and disintegrations of them seem to continue up to near $x/r_0 = 12$. Velocity and pressure fluctuations caused by these disintegrations are discussed at following sections.

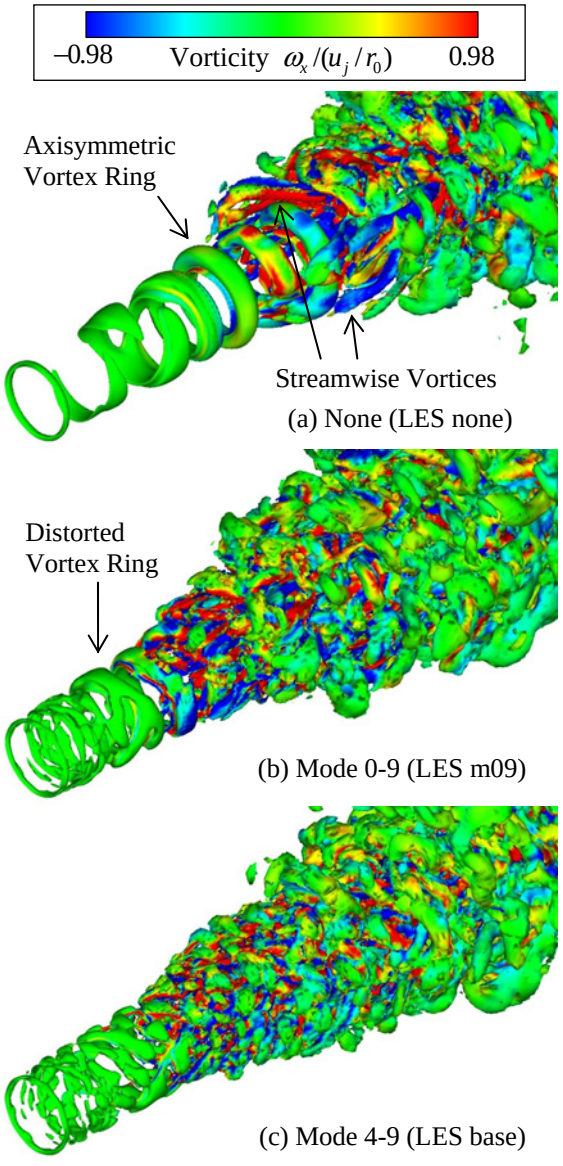

Fig. 6 Iso-surfaces of Q colored according to ω_x

Velocity Fluctuations at the Shear Layer

Axial profiles of the root mean square values of the radial fluctuating velocities along the shear layer ($r = r_0$), Ur'_{rms}, are plotted in Fig. 7.

In the region with $x/r_0 < 5$, Ur'_{rms} for all cases increases with increasing x. This is because the unsteadiness of the shear layer increases with increasing x, which is confirmed by the vortex structures. In this region, Ur'_{rms} for the cases with the inflow forcing are larger than that for without it. This is due to the characteristic of the inflow forcing that introduces unsteadiness around the shear layer.

In the downstream region, where the vortices developed at the shear layer disintegrate into small ones, the maximal value of Ur'_{rms} without inflow forcing is larger than that with the inflow forcing. The position with the maximal value is approximately $x/r_0 = 9$ unlike that of the other cases with peak positions at $5 < x/r_0 < 7$. Comparison between the two different modes cases shows that Ur'_{rms} is larger for Mode 0-9 than for Mode 4-9.

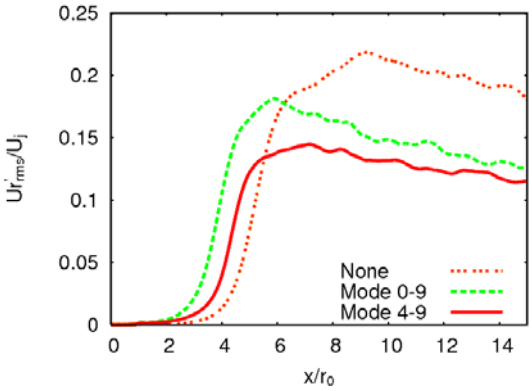

Fig. 7 Axial profiles of the root mean square values of the radial fluctuating velocities along the shear layer

Near-Field Pressure Fluctuations

Relations between the vortex structures and the pressure fluctuations are discussed. Fig. 8 shows instantaneous values of ω_z and OASPL, which is used here to represent the magnitude of pressure fluctuation. For the case without inflow forcing, vortex rings interact with each other at the region from about $x/r_0 = 5$ to 9, where OASPL becomes maximal value 176.7 dB. In addition to this region, pressure fluctuations at the region from about $x/r_0 = 9$ to 15, where vortices break down and disintegrate, are considerably large compared with the other cases. By contrast, for the case with inflow forcing, pressure fluctuations accompanied with interaction and disintegration of vortices, are significantly smaller than without inflow forcing. OASPL for Mode 4-9 is smaller than that for Mode 0-9 at almost whole region. The maximum value of OASPL is 174.6 dB for Mode 0-9 and 169.9 dB for Mode 4-9.

Role of Inflow Forcing

From these results obtained above, the role of inflow forcing can be clarified. Without inflow forcing, axiymmetric vortices develop at the shear layer. They interact with each other and disintegrate. At that time, the vortex motions induce high amplitude velocity and pressure fluctuations, which would generate high-intensity sound waves. That is the reason why the jet develops rapidly and the far-field SPL are overestimated compared to that of experiments. On the contrary, inflow forcing breaks down the unphysical axiymmetric vortices and avoids them from generating the high amplitude velocity and pressure fluctuations. This is the reason why the inflow forcing reduced the differences between calculation results and experimental results on both the flow and sound field. The effect to reduce the overestimation of the velocity and pressure fluctuations is larger when low modes are cut than when not, and has no significant dependence on the forcing amplitude or the application range. This is due to the role that the inflow forcing breaks down unphysical axisymmetric vortex rings.

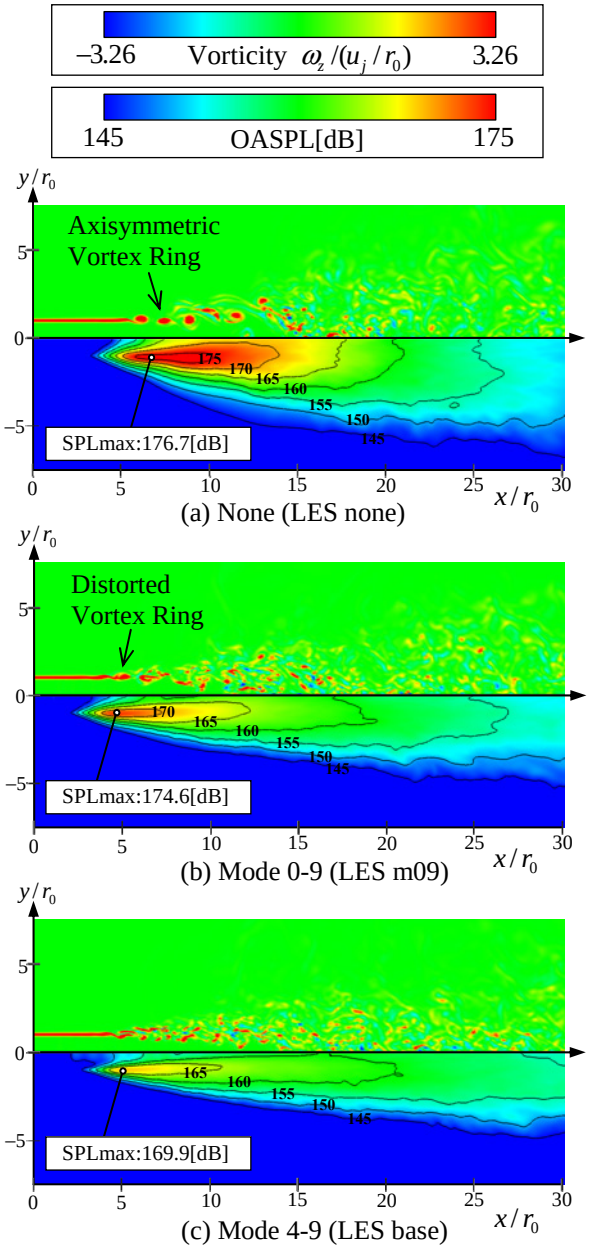

Fig. 8 Contours of ω_z (top) and OASPL (bottom)

Noise Generation Analysis

Dominant jet noise and its generation mechanism are analyzed for the case: LES narrow of which results are in a good agreement with experiments.

Dominant Jet Noise

The dominant jet noise has a peak at an angle of 30 to 40 degrees, which was confirmed by Fig. 5. For analyzing the dominant frequency of this dominant noise, wavelet transformation is applied to the pressure data at $x/r_0 = 27.5$ and $r/r_0 = 9.7$. Then, $\left|X_{wav}(a,b)/\sqrt{a}\right|$ is here calculated as an indicator of the magnitude of the acoustic pressure fluctuations so that waves with same amplitude but different frequency indicate the same values. $\left|X_{wav}(a,b)/\sqrt{a}\right|$ averaged over $\theta = 0$ to 2π in the circumferential direction is shown in Fig. 9. This result shows that a frequency range approximately from $St = 0.2$ to 0.4 is dominant for most of the high-amplitude noise. This frequency range is consistent with previous results[1-5].

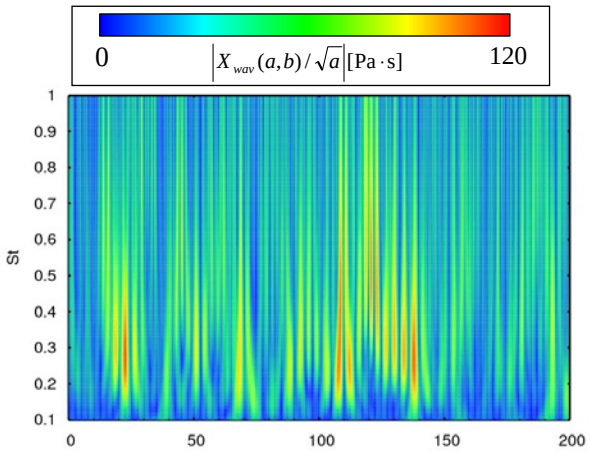

Fig. 9 Wavelet transformation of pressure

Noise Source Locations

The sources of the dominant noise are located using the virtual microphone array and the beamforming algorithm. The pressure fluctuations are recorded by the virtual microphones located downstream. Then wavelet transformation with a time scale corresponding to $St = 0.3$, are applied to them. Twelve source locations of the noise with amplitude exceeding 1.5σ are plotted in Fig. 10. Time-averaged streamwise velocity contour is also shown in this figure to compare them with the flow field. These source locations are distributed approximately from $x/r_0 = 9$ to 14. In this simulation, the distribution of the time-averaged streamwise velocity along the centerline is shown in Fig. 3 (LES narrow) and the length of the jet potential core, x_c, is $x_c/r_0 = 14.0$ when the length x_c is defined so as to satisfy $\bar{u}_c(x_c) = 0.95u_j$.

These results suggest that the dominant jet noise generates from the region near the end of the jet potential core. This is also consistent with other workers' results[6-11].

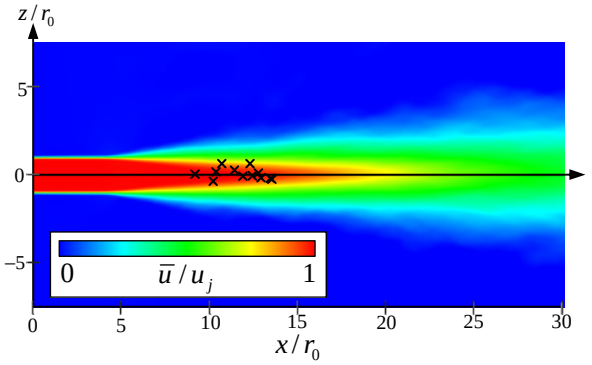

Fig. 10 Source locations of the dominant noise

Relation between vortices and pressure

Since the sources of the dominant noise are located near the end of the jet potential core, relation between vortices and pressure near this region is investigated. Instantaneous absolute values of vorticity vector, $|\boldsymbol{\omega}|$, and pressure are shown in Fig. 11a, where $|\boldsymbol{\omega}|$ is shown at only the region with $|\boldsymbol{\omega}|/(u_j/r_0) \geq 4$. Enlarged view of it near the end of the jet potential core, here an region with $5 \leq x/r_0 \leq 20$, is shown in Fig. 11b. This region corresponds approximately to the region where the amplitude of pressure fluctuation is higher than 160 dB in Fig. 8c.

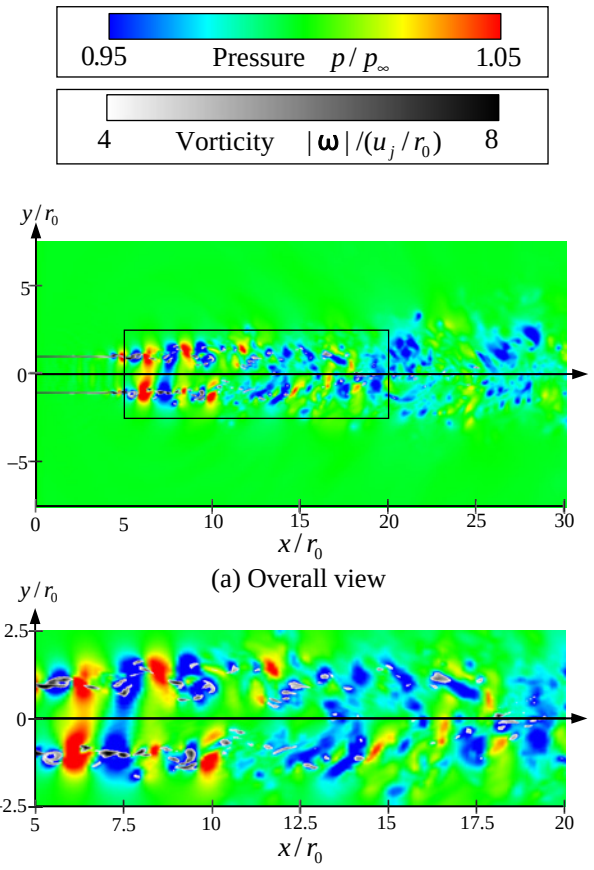

(a) Overall view

(b) Near the end of the jet potential core

Fig. 11 Instantaneous pressure and vorticity

From Fig. 11, it can be seen that there are many areas with locally high or low pressure. Especially in the region with $5 \le x/r_0 \le 20$, the magnitude of the local pressure fluctuation is higher than in the outer region. Furthermore, comparison with vorticity and pressure shows that pressure becomes low locally at the area where the vorticity is strong or where some vortices interact with each other, and becomes comparatively high where not. This result indicates that these vortex motions induce pressure fluctuation locally. Consequently, it is confirmed that noise generation can be ascribed to the vortex motions.

In the region with $5 \le x/r_0 \le 10$, vortex structures with high circumferential coherence are formed, yielding to a characteristic pressure distribution that is composed of alternately positive and negative pressures regions along the streamwise distance. In the region downstream from it, since the shear layers interact at near the centerline and yield many small-scale vortices, the vortex structures and the pressure distribution appears to be complicated.

Noise Generation Mechanism

Since it is confirmed above that the vortex motions cause the pressure fluctuations, dominant structure of these pressure fluctuations are discussed here. Wavelet transformation is applied to the pressure using a time scale corresponding $St = 0.3$. The result is shown in Fig. 12 for two different contour ranges.

Fig. 12a shows that the dominant pressure fluctuations are not randomly distributed but well organized. In addition, it is clarified that this well organized distribution takes a train of alternately positive and negative wavelet-transformed pressure regions along the jet distance, covering the almost whole near-field. The time evolution of this pressure fluctuation structure indicates that this structure with the region downstream or outside from the dashed black lines spreads towards the downstream, keeping the cross-streamwise coherence. As it spreads towards the downstream, it becomes like spherical wave fronts, resulting in the dominant jet noise which was shown above in Fig. 9. On the other hand, the pressure fluctuation structure with the region upstream from the dashed black lines moves to the upstream.

Fig. 12b indicates that compared to the outer region, the dominant pressure fluctuations are high especially in the region with $5 < x/r_0 < 25$, which contains the end of the jet potential core and the noise source locations obtained above. In addition, as shown above in Fig. 11, this region corresponds to the region where vortices grown in the shear layer interact with each other and disintegrate into small ones.

From these results, we can understand the noise generation mechanism as follows. The shear layers interact with each other and disintegrate into small ones mainly at the region near the end of the jet potential core. At this region, relatively violent vortex motions induce pressure fluctuations. Though this phenomenon seems to be complicated, the dominant structure of these pressure fluctuations is well organized. This structure takes a train of alternately positive and negative wavelet-transformed pressure regions along the jet distance, and then spreads to the downstream by the effects of advection and propagation, keeping its cross-stream coherence. This mechanism is the reason why a high subsonic jet produces the dominant noise with the particular downstream directivity.

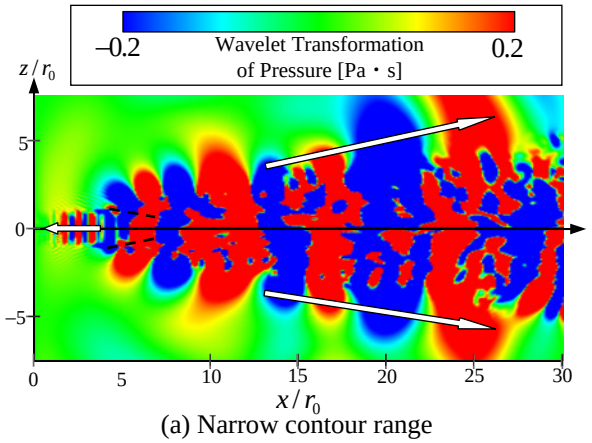

(a) Narrow contour range

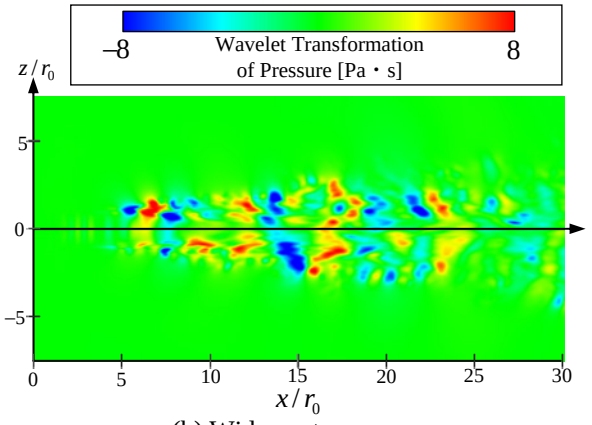

(b) Wide contour range

Fig. 12 Dominant pressure fluctuations obtained by wavelet transformation

Conclusion

High subsonic jets were computed using compressible Large Eddy Simulation.

(1) Influences of the inflow forcing on the flow and sound field were investigated by comparing the results of its parameters. It was clarified that inflow forcing has an important role to break down unphysical axiymmetric vortices that cause high amplitude velocity and pressure fluctuations. By this effect, inflow forcing reduces overestimation of the jet development and the far-field SPL.

(2) The generation mechanism of the dominant jet noise was investigated by applying wavelet transformation to the pressure data. It was confirmed that relatively violent vortex motions induce pressure fluctu-

ations at the region near the end of the jet potential core, where shear layers interact with each other and disintegrate into small ones. The dominant structure of these pressure fluctuations turned out to be well organized. Furthermore, it was clarified that this structure takes a train of alternatively positive and negative wavelet-transformed pressure regions along the jet distance. Then, this structure spreads towards the downstream by the effects of advection and propagation, keeping its cross-stream coherence. This mechanism is the reason why a high subsonic jet produces the dominant noise with the particular downstream directivity.

References

1) Mollo-Christensen, E., Kolpin, M. A., and Martuccelli, J. R.: Experiments on Jet Flows and Jet Noise Far-Field Spectra and Directivity Patterns, *Journal of Fluid Mechanics*, **18**, 1964, pp. 285-301.
2) Tanna, H. K.: An Experimental Study of Jet Noise Part 1: Turbulent Mixing Noise, *Journal of Sound and Vibration*, **50**(3), 1977, pp. 405-428.
3) Tam, C. K. W.: Jet Noise Generated by Large-Scale Coherent Motion, *Aeroacoustics of Flight Vehicles: Theory and Practice. Volume 1: Noise Sources*, 1991, pp.311-390.
4) Simonich J., Narayanan S., Barber T. J., and Nishimura, M.: Aeroacoustic Characterization Noise Reduction and Dimensional Scaling Effects of High Subsonic Jets, *AIAA Journal*, **39**, 2001, pp. 2062-2069.
5) Viswanathan, K.: Aeroacoustics of Hot Jets, *Journal of Fluid Mechanics*, **516**, 2004, pp.39-82.
6) Fisher, M. J., Harper-Bourne, M., and Glegg, S. A. L.: Jet Engine Source Location: the Polar Correlation Technique, *Journal of Sound and Vibration*, **51**, 1977, pp. 23-54.
7) Morrison, G. L. and McLaughlin, D. K.: Noise Generation by Instabilities in Low Reynolds Number Supersonic Jets, *Journal of Sound and Vibration*, **65**(2), 1979, pp.177-191.
8) Schaffar, M.: Direct Measurements of the Correlation between Axial In-jet Velocity Fluctuations and Far-Field Noise Near the Axis of a Cold Jet, *Journal of Sound and Vibration*, **64**, 1979, pp.73-83.
9) Freund, J. B.: Noise Sources in a Low-Reynolds Number Turbulent Jet at Mach 0.9, *Journal of Fluid Mechanics*, **438**, 2001, pp.277-305.
10) Narayanan, S., Barber, T. J., and Polak, D. R.: High Subsonic Jet Experiments: Turbulence and Noise Generation Studies, *AIAA Journal*, **40**(3), 2002, pp.430-437.
11) Venkatesh, S. R., Polak, D. R., and Narayanan, S.: Beamforming Algorithm for Distributed Source Localization and Its Application to Jet Noise, *AIAA Journal*, **41**(7), 2003, pp.1238-1246.
12) Lighthill, M. J.: On Sound Generated Aerodynamically 1. General Theory, *Proc. of the Royal Society of London*, **A**(211), 1954, pp. 564-587.
13) Powell, A.: Theory of Vortex Sound, *Journal of Acoustical Society of America*, **36**(1), 1964, pp.177-195.
14) Mollo-Christensen, E.: Jet Noise and Shear Flow Instability Seen from an Experimenter's Viewpoint, *Trans. A. S. M. E. Journal of Applied Mechanics*, **34**, 1967, pp.1-7.
15) Crow, S. C., and Champague, F. H.: Orderly Structure in Jet Turbulence, *Journal of Fluid Mechanics*, **48**, 1971, pp.547-591.
16) Brown, G. L., and Roshko, A.: On Density Effects and Large Structure in Turbulent Mixing Layers, *Journal of Fluid Mechanics*, **64**, 1974, pp.775-816.
17) Crow, S. C.: Acoustic Gain of a Turbulent Jet, *Bull. Am. Phys. Soc. IE6*, 1972.
18) Laufer, J. Kaplan, R. E., and Chu, W. T.: On the Generation of Jet Noise, *AGARD CP-131 on Noise mechanism*, 1973.
19) Laufer, J.: On the Mechanism of Noise Generation by Turbulence, *Univ. South. Calif., Aerospace Engng.*, **125**, 1974.
20) Hileman, J., and Samimy, M.: Turbulence Structures and the Acoustic Far Field of a Mach 1.3 Jet, *AIAA Journal*, **39**(9), 2001, pp.1716-1727.
21) Hileman, J., Thurow, B., and Samimy, M.: Development and Evaluation of a 3-D Microphone Array to Locate Individual Acoustic Sources in a High-Speed Jet, *Journal of Sound and Vibration*, **276**, 2004, pp. 649-669.
22) Hileman, J., Thurow, B., Caraballo, E., and Samimy, M.: Large-Scale Structure Evolution and Sound Emission in High-Speed Jets: Real-Time Visualization with Simultaneous Acoustic Measurements, *Journal of Fluid Mechanics*, **544**, 2005, pp.277-307.
23) Kastner, J., Samimy, M., Hileman, J., and Freund, J. B.: Comparison of Noise Mechanisms in High and Low Reynolds Number High-Speed Jets, *AIAA Journal*, **44**(10), 2006, pp.2251-2258.
24) Bodony, D. J., and Lele, S. K.: Review of the Current Status of Jet Noise Predictions Using Large-Eddy Simulation (invited), AIAA Paper 2006-0468.
25) Bogey, C., Bailly, C., and Juve, D.: Noise Investigation of a High Subsonic, Moderate Reynolds Number Jet Using a Compressible Large Eddy Simulation, *Theoretical and Computational Fluid Dynamics*, **16**(4), 2003, pp. 273-297.
26) Bogey, C., and Bailly, C.: LES of a High Reynolds, High Subsonic Jet: Effect of the Inflow Conditions on Flow and Noise, AIAA Paper 2003-3170.
27) Lew, P., Uzun, A., Blaisdell, G. A., and Lyrintzis, A. S.: Effects of Inflow Forcing on Jet Noise Using Large Eddy Simulation, AIAA Paper 2004-0516.
28) Germano, M., Piomelli, U., Moin, P., and Cabot, W. H.: A Dynamic Subgrid-Scale Eddy Viscosity

Model, *Physics of Fluids*, **3**(7), 1991, pp.1760-1765.
29) Moin, P., Squires, W., Cabot, W., and Lee, S.: A Dynamic Subgrid-Scale Model for Compressible Turbulence and Scalar Transport, *Physics of Fluids A*, **3**(11), 1991, pp.2746-2757.
30) Lilly, D. K.: A Proposed Modification of the Germano Subgrid-Scale Closure Method, *Physics of Fluids A*, **4**(3), 1992, pp.633-635.
31) Lele, S. K.: Compact Finite Difference Schemes with Spectral-like Resolution, *Journal of Computational Physics*, **103**(1), 1992, pp.16-42.
32) Gaitonde, D. V., and Visbal, M. R.: Pade-Type Higher-Order Boundary Filters for the Navier-Stokes Equations, *AIAA Journal*, **38**(11), 2000, pp.2103-2112.
33) Thompson, K. W.: Time Dependent Boundary Conditions for Hyperbolic Systems, *Journal of Computational Physics*, **68**, 1987, pp.1-24.
34) Thompson, K. W.: Time Dependent Boundary Conditions for Hyperbolic Systems 2, *Journal of Computational Physics*, **89**, 1990, pp.439-461.
35) Freund, J. B.: Proposed Inflow / Outflow Boundary Condition for Direct Computation of Aerodynamic Sound, *AIAA Journal*, **3**5(4),1997, pp.740-742.
36) Mohseni, T., and Colonius, T.: Numerical Treatment of Polar Coordinate Singularities, *Journal of Computational Physics*, **157**(2), 2000, pp.787-795.
37) Pan, F. L., Uzun, A., and Lyrintzis, A. S.: Refraction Corrections for Surface Integral Methods in Jet Aeroacoustics, AIAA Paper 2004-2873.
38) Lyrintzis, A.: Review: The Use of Kirchhoff's Method in Computational Aeroacoustics, *ASME Journal of Fluids Engineering*, **116,** 1994, pp. 665-676.
39) Freund, J., Lele, S., and Moin, P.: Calculation of the Radiated Sound Field Using an Open Kirchhoff Surface, *AIAA Journal*, **34**(5), 1996, pp.909-916.
40) Rahier, G., Prieur, J., Vuillot, F., Lupoglazoff, N., and Biancherin, A.: Investigation of Integral Surface Formulations for Acoustic Predictions of Hot Jets Starting from Unsteady Aerodynamic Simulations, AIAA Paper 2003-3164.
41) Daubechies, I.: Ten Lectures on Wavelets, Society for Industrial and Applied Mathematics, Philadelphia, 1992, pp.1-106.
42) Lewalle, J.: Wavelet Analysis of Experimental Data : Some Method and the Underlying Physics, AIAA Paper 94-2281.
43) Wang, Q., Brasseur, J., Smith, R., and Smits, A.: Application of the Multi-Dimensional Wavelet Transforms to the Analysis of Turbulent Data, *International Workshop on Wavelets*, Springer-Verlag, New-York, 1991.
44) Lau, J. C., Morris, P. J., and Fisher, M. J.: Measurements in Subsonic and Supersonic Free Jets Using a Laser Velocimeter, *Journal of Fluid Mechanics*, **285**, part 1, 1995, pp.1-27.
45) Stromberg, J. L., McLaughlin, D. K., and Trout, T. R.: Flow field and Acoustic Properties of a Mach Number 0.9 Jet at a Low Reynolds Number, *Journal of Sound and Vibration*, **72**, 1980, pp.159-176.
46) Lush, P. A.: Measurements of Subsonic Jet Noise and Comparison with Theory, *Journal of Fluid Mechanics*, **46**, 1971, pp.477-500.
47) Jeong, J., and Hussain, F.: On the Identification of a Vortex, *Journal of Fluid Mechanics*, **285**, 1995, pp. 69-94.